Communications Physics

https://doi.org/10.1038/s42005-026-02530-w

Article in Press

Learning hadron emitting sources with deep neural networks

Received: 17 February 2025

Accepted: 28 January 2026

Cite this article as: Wang, L., Zhao, J. Learning hadron emitting sources with deep neural networks. *Commun Phys* (2026). https://doi.org/10.1038/s42005-026-02530-w

Lingxiao Wang & Jiaxing Zhao

Learning Hadron Emitting Sources with Deep Neural Networks

Lingxiao Wang[1] **and Jiaxing Zhao**[2,3*]

[1]Interdisciplinary Theoretical and Mathematical Sciences Program (iTHEMS), RIKEN Wako, Saitama 351-0198, Japan
[2]Helmholtz Research Academy Hesse for FAIR (HFHF), GSI Helmholtz Center for Heavy Ion Physics, Campus Frankfurt, 60438 Frankfurt, Germany
[3]Institut für Theoretische Physik, Johann Wolfgang Goethe-Universität,Max-von-Laue-Straße 1, D-60438 Frankfurt am Main, Germany
[*]jzhao@itp.uni-frankfurt.de

ABSTRACT

The correlation function observed in high-energy collision experiments encodes critical information about the emitted source and hadronic interactions. While the proton-proton interaction potential is well constrained by nucleon-nucleon scattering data, these measurements offer a unique avenue to investigate the proton-emitting source, reflecting the dynamical properties of the collisions. In this context, the understanding of other hadronic interactions such as hyperon–nucleon remains limited. In this work, we present an unbiased approach to reconstruct proton-emitting sources from experimental correlation functions. Within an automatic differentiation framework, we parameterize the source functions with deep neural networks, to compute correlation functions. This approach achieves a lower chi-squared value compared to conventional Gaussian source functions and captures the long-tail behavior, in qualitative agreement with simulation predictions. We finally apply our method to extract hyperon–nucleon correlations.

Introduction

Nuclear forces, also referred to as strong forces, are the forces that act between two or more nucleons (nuclei), which bind the nucleons (nuclei) together. The nuclear force between two nucleons is generated by mediating the π meson, as first proposed by H. Yukawa[1]. Following the experimental discovery of the heavier mesons, namely the σ, $\rho(770)$, and $\omega(782)$, the Yukawa theory was extended to the one-boson-exchange (OBE) model[2,3]. There are numerous OBE-based/extended phenomenological nucleon-nucleon (N-N) potentials exist, including the Paris potential[4], the *Argonne*-18 potential (Av-18)[5], the Reid Soft-Core potential[6], the Nijmegen potentials[7,8], and so on. The parameters in these forms are determined by explaining the N-N elastic scattering data. Moreover, the chiral effective field theory approach is derived from the principles of Quantum Chromodynamics (QCD) using chiral perturbation theory to investigate the nuclear force[9–14], which systematically consider the symmetries of QCD and provide a framework for including multi-nucleon forces. Additionally, the nuclear forces can also been extracted from the first-principles approach, namely lattice QCD[15–19].

So far, we already have a better understanding of the N-N interaction. However, our comprehension of other interactions, such as those involving mesons and hyperons, remains limited. The clarification of these nuclear forces facilitates not only an understanding of the formation and reaction of nuclei, but also an understanding of the behavior of QCD matter at the most fundamental level. Meanwhile, the nuclear force plays a critical role in the evolution of stellar and supernova explosions, the formation of heavy elements in the universe, and the characteristics of neutron stars[20].

One effective experimental method for investigating hadronic interactions is the femtoscopy, which is inspired by the Hanbury Brown and Twiss (HBT) correlation[21–23]. Femtoscopy method was utilized to probe the space-time configuration of the system at freeze-out[23–29]. The femtoscopy technique relates the final two-body correlation to the two-body interaction[23]. In accordance with the formalism of femtoscopy, the correlation function observed in the experiment can be calculated theoretically by convoluting the source function $S(\boldsymbol{r})$ with the two-body scattering wavefunction $\psi_k(\boldsymbol{r})$ via,

$$C(k) = \int S(\boldsymbol{r})|\psi_k(\boldsymbol{r})|^2 d\boldsymbol{r}, \tag{1}$$

where $k = |\mathbf{p}_1 - \mathbf{p}_2|/2$ is the relative momentum in the center-of-mass frame of the pair, and $\mathbf{r}$ is the relative distance between the two particles. The two-body scattering wave function $\psi_k(\mathbf{r})$ can be obtained by solving the Schrödinger equation. This has been done in two popular tools that are the Correlation Afterburner (CRAB)[30] and the Correlation Analysis Tool using the Schrödinger equation (CATS)[31,32].

Benefit from advanced experimental conditions, many two-hadrons correlations have been observed in both proton-proton and heavy-ion collisions in the Relativistic Heavy Ion Collider (RHIC)[33–36] and the Large Hadron Collider (LHC)[37–41]. This provides an excellent opportunity to study hadronic interactions. In experiments, the Lednický and Lyuboshits model[37,42,43] has consistently been employed to describe correlation functions, that assume a Gaussian source function and the interaction is encoded in the scattering length, a_0,

and the effective range, $r_{\rm eff}$, which are based on a short-range interaction approximation. Nevertheless, many previous theoretical[26,27,44–46] and experimental[47–53] studies have shown that the hadron-emitting source exhibits significant deviations from a purely Gaussian shape. A precise emission source is indispensable for probing hadronic interactions with high accuracy, particularly nucleon–hyperon, hyperon-hyperon forces, which are weakly constrained by scattering experiments and complementary approaches such as lattice QCD. Second, it offers valuable constraints on hadronic dynamics and hadron coalescence mechanisms. Given the growing availability of high-precision correlation data, the extraction of an accurate emission source is both timely and highly worthwhile. Benefiting from the well-established knowledge of the proton–proton interaction, in this work we perform an unbiased analysis to precisely determine the hadron-emitting source directly from experimental data.

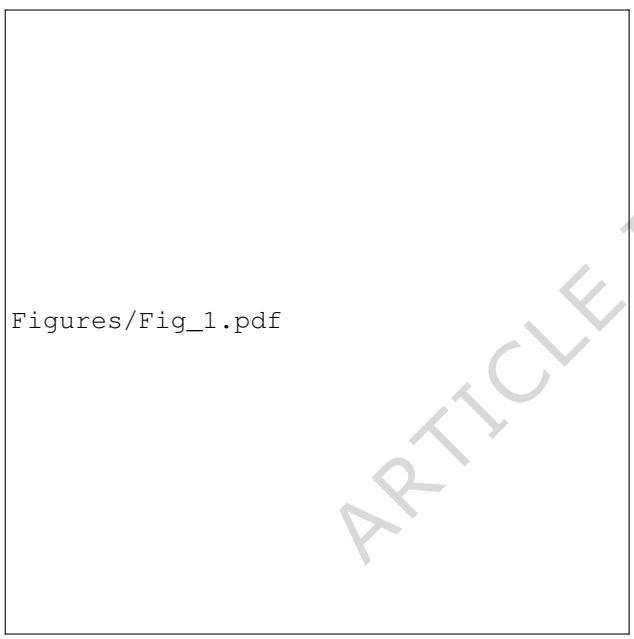

Figure 1. The interaction potentials and the scattering wavefunction square between proton-proton pairs. The proton-proton interaction potential is shown in (a) and the scattering wavefunction square at $k = 19.5$ MeV/c is shown in (b). The red and blue lines represent the Av-18 and Reid potential, respectively. The solid lines indicate the spin-singlet state, while the dashed lines depict the spin-triplet state.

Results

As previously noted, the proton-proton interaction potential has been built by fitting the N-N scattering data. In this study, we consider two commonly used pp potentials: the Reid potential[7,54] and the Av-18 potential[5], as shown in the panel (a) of Fig. 1. These potentials include only strong interactions, with tensor interactions excluded. It can be observed that both the Av-18 and Reid potentials exhibit a pronounced repulsive core at short range, which gradually diminishes to zero at long range due to one-pion exchange. The intermediate range, defined as $1 < r < 2$fm, is attributed to the exchange of scalar and vector mesons. Considering the spin configuration, the interaction potentials are categorized as either spin-singlet or spin-triplet. For the spin-singlet state, the Av-18 and Reid potentials are observed to be in close agreement. However, a significant difference is evident in the spin-triplet state, as depicted by the dotted lines.

In experiments, it is insufficient to distinguish between the spin-singlet and spin-triplet states, necessitating consideration of contributions from both. The relative contributions are determined by the spin degeneracy. Consequently, the correlation function given in Eq. (1) can be expressed as,

$$C(k) = \int S(\boldsymbol{r}) \left(\frac{1}{4} |\psi_k^{S=0}(\boldsymbol{r})|^2 + \frac{3}{4} |\psi_k^{S=1}(\boldsymbol{r})|^2 \right) d\boldsymbol{r}, \quad (2)$$

where the spin-singlet wave function $\psi_k^{S=0}(\boldsymbol{r})$ and the spin-triplet scattering wave function $\psi_k^{S=1}(\boldsymbol{r})$ are calculated by solving the Schrödinger equation with the aforementioned potential. The radial Schrödinger equation for the scattering states is,

$$\frac{d^2 u_{k,l}^S(r)}{dr^2} = \left(2\mu V(r) + \frac{l(l+1)}{r^2} - k^2 \right) u_{k,l}^S(r), \quad (3)$$

where $\mu = m_p/2$ is the reduced mass, and $u_{k,l}^S(r)$ represents the radial wave function for spin state S in $l-$wave scattering. For low-energy scattering, the $S-$wave channel dominates. However, as the energy increases, contributions from higher-order spin channels become significant.

Consequently, the total scattering wavefunction can be expressed as follows,

$$\psi_k^S(\mathbf{r}) = \sum_{l=0}^{l_{\rm max}} (2l+1) i^l \frac{u_{k,l}^S(r)}{r} P_l(\cos\theta), \quad (4)$$

where P_l denotes the Legendre polynomials. For low-energy scattering, the series converges relatively rapidly. In this study, we set $l_{\rm max} = 3$, and utilized the CATS to solve the Schrödinger equation[31,32]. The convergence of the series was verified. The scattering wavefunctions are shown in the panel (b) of Fig. 1, where it is evident that the spin-singlet wavefunction is significantly larger than the spin-triplet wavefunction.

The correlation function (CF), $C(k)$, can be obtained by convolving the scattering functions with the estimated source function (SF). The isotropic Gaussian function is the most commonly used form[55]. Its functional form is given by Eq. (5), where the radius r_0 serves as the controlling parameter for the source size,

$$S(r) = \frac{1}{(4\pi r_0^2)^{3/2}} \exp\left(-\frac{r^2}{4r_0^2} \right). \quad (5)$$

However, many studies have shown that the SF significantly deviates from the Gaussian *Ansatz* with resonance contributions[26,27,50]. This deviations is even more pronounced in

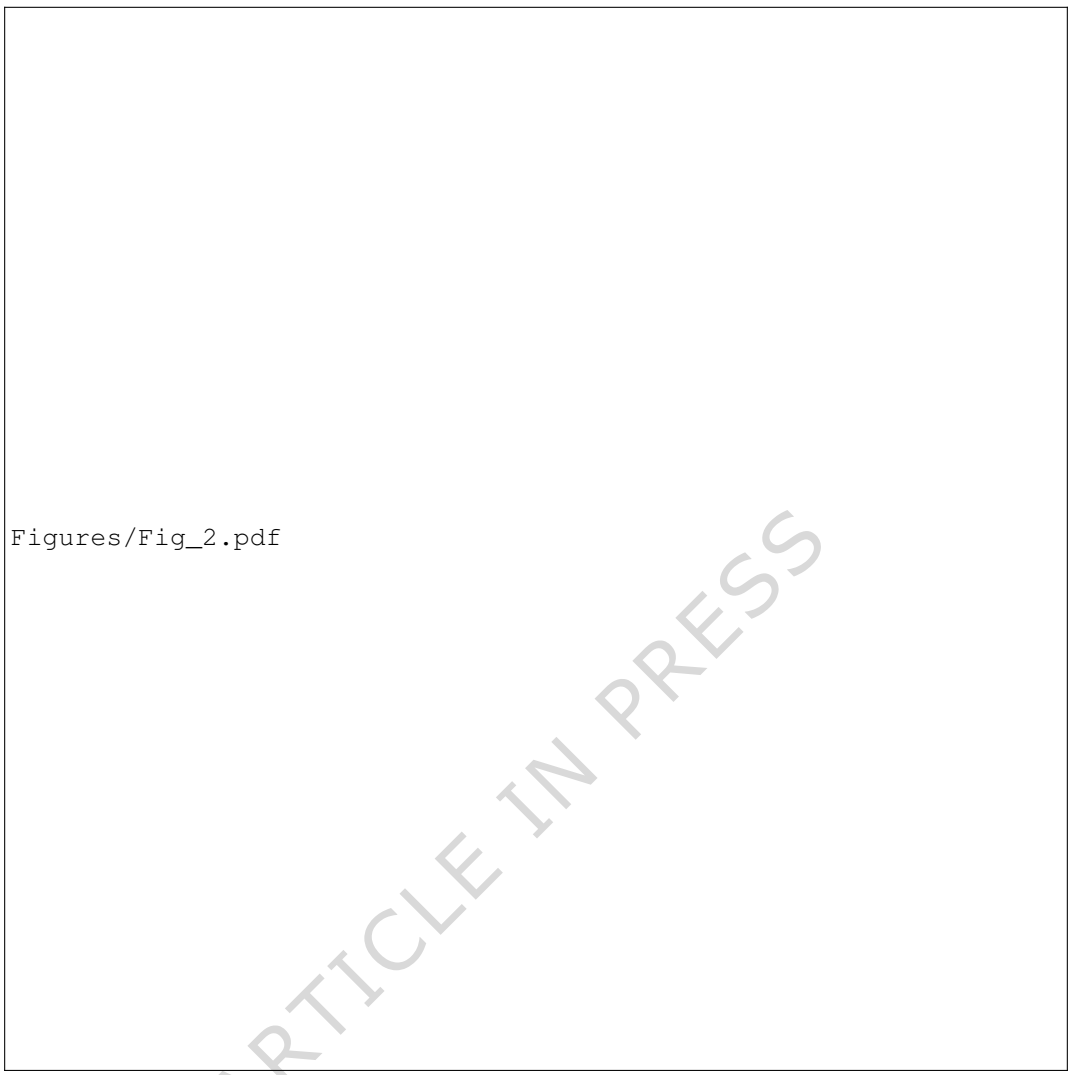

Figure 2. Reconstruction of source functions from correlation functions using a neural-network mapping. A neural network takes radial distance r as input (grey squares) and outputs the source function values $S_\theta(r_i)$ (red squares) at discretized points. These outputs are combined with known kernel functions $|\psi_k(r_i)|^2$ (blue squares) via convolution to produce predicted correlation functions $C(k_j) = \sum_i^{N_r} \Delta r\, S_\theta(r_i)\, |\psi_k(r_i)|^2$ (yellow squares). The predicted results are compared with observed data C_i (black squares) to compute the loss function $\mathscr{L} = \sum_j^{N_k} (C(k_j) - C_j)^2/\text{error}_j^2$. The gradients $\partial\mathscr{L}/\partial\theta$ are then used to optimize the network parameters, $\{\theta\}$.

small collision systems such as pp collisions[47]. A solid modeling of the strong resonance contribution to the source function is imperative, yet currently lacking. Such deviations can introduce non-negligible biases when attempting to understand hadron-hadron interactions through Femtoscopy. From an inverse problem perspective[56], we propose an automatic differentiable framework illustrated in Fig. 2, to reconstruct an unbiased source function directly from correlation functions. Here, an isotropic source approximation is adopted for pp collisions, which is advantageous for smaller systems due to the absence of evident collective flow.

In our framework, the SF is from outputs of a deep neural network (DNN) *Ansatz*, collected as $\vec{S} = [S_1, S_2, \cdots, S_{N_r}]$. It is illustrated with red squares in Fig. 2. The correlation function can be calculated as,

$$C(k) = \sum_i^{N_r} S_i |\psi_k(r_i)|^2 \Delta r, \tag{6}$$

where N_r is the number of discrete radii and Δr is the step size of the wavefunction. As shown in Fig. 2, after the forward process of the network and convolution, we obtain $\vec{S}$ and subsequently compute the reconstruction error as the loss function,

$$\mathscr{L} = \sum_i^{N_k} (\mathrm{C}_i - C(k_i))^2/\sigma_i^2, \tag{7}$$

where C_i represents the measured CF at k_i with N_k points, and σ_i^2 denotes the variance assigned to each uncorrelated observation in the standard χ^2 function. Furthermore, this approach can be extended to multi-source observations by summing over them.

To optimize the parameters of the network representations, $\{\boldsymbol{\theta}\}$, with the loss function, we employ gradient-based algorithms. The gradient of the loss function is derived as,

$$\nabla_{\boldsymbol{\theta}}\mathscr{L} = \sum_{i,j} |\psi_{k_j}(r_i)|^2 \frac{\partial \mathscr{L}}{\partial C(k_j)} \nabla_{\boldsymbol{\theta}} S_{\boldsymbol{\theta}}(r_i), \tag{8}$$

where $\nabla_{\boldsymbol{\theta}} S_{\boldsymbol{\theta}}(r_i)$ is computed using the standard backpropagation (BP) method in deep learning[57]. The reconstruction error is propagated through each layer of the neural network, and, combined with gradients derived via automatic differentiation, these are used to optimize the network parameters.

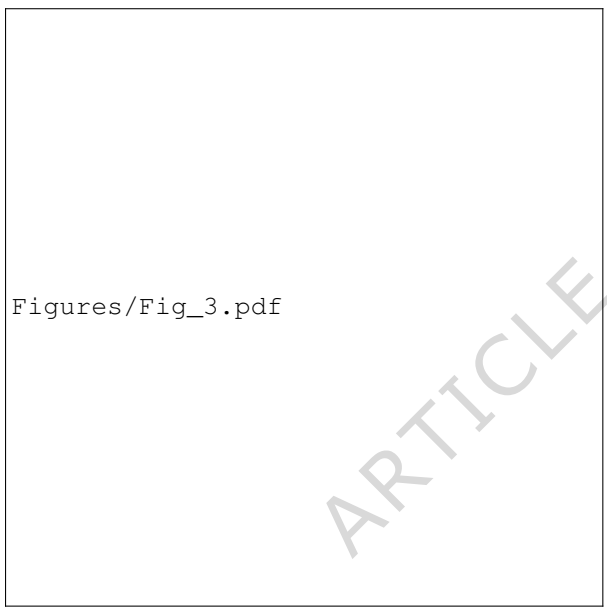

Figure 3. Emission sources and proton-proton correlation functions using a Gaussian or neural network source with the Reid potential. The comparison of the emission sources is shown in (a). Panel (b) shows the proton-proton correlation functions with different emission sources. The red line corresponds to the Neural Network *Ansatz*, while the blue line represents the Gaussian source with $r_0 = 1.32$ fm. The shaded red band corresponds to the 68% Confidence Level (CL) uncertainty. The experimental data (black dots) are obtained from pp collisions at $\sqrt{s} = 7$ TeV by the ALICE collaboration[37].

The proton-proton CF can be obtained by convolving the scattering functions with the Gaussian source as Eq. (5), and the Neural Network source, as illustrated in Fig. 3 (a) with the Reid potential and Fig. 4 (a) with the Av-18 potential.

The width r_0 of the Gaussian source is obtained by minimizing the chi-squared value relative to the experimental data,

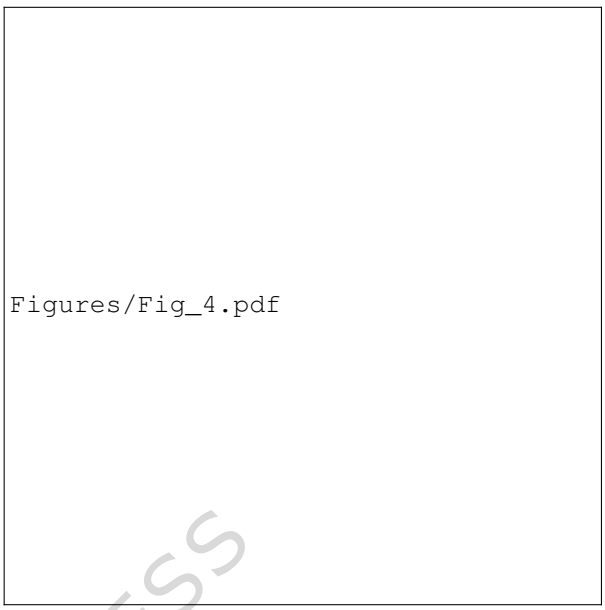

Figure 4. Emission sources and proton-proton correlation functions using a Gaussian or neural network source with the Av-18 potential. The comparison of the emission sources is shown in (a). Panel (b) shows the proton-proton correlation functions with different emission sources. The red line corresponds to the Neural Network *Ansatz*, while the blue line represents the Gaussian source with $r_0 = 1.26$ fm. The shaded red band corresponds to the 68% Confidence Level (CL) uncertainty. The experimental data (black dots) are obtained from pp collisions at $\sqrt{s} = 7$ TeV by the ALICE collaboration[37].

yielding $r_0 = 1.32$ fm for the Reid potential ($\chi^2 = 90.72$) and $r_0 = 1.26$ fm for the Av-18 potential ($\chi^2 = 89.12$). It is evident that the CF cannot be accurately reproduced across the full range of relative momentum in either case using the optimized Gaussian sources. In contrast, the SF constructed by the neural network ($\chi^2 = 34.55$ for the Reid potential and $\chi^2 = 35.81$ for the Av-18 potential) provides an adequate description of the experimental data, except for the first data point, which exhibits a significant degree of uncertainty and lies outside the predicted range, as shown in Fig. 3 (b) and Fig. 4 (b) with red curves. A visual inspection of the SF reveals that it adopts a non-Gaussian form with a pronounced "tail". Such behavior of the SF may be caused by strong resonance contributions, as suggested in previous studies[26,27,44–46]. This effect is even more pronounced in small collision systems such as proton-proton and proton-lead collisions[47–53]. In Ref.[49], the SF is constructed by incorporating the effects of short-lived resonances, resulting in a non-Gaussian shape. The exponential nature of resonance decays manifests as exponential tails in the source distribution. Inspired by this framework, a source distribution for baryons is built starting from two components: a Gaussian core and a non-Gaussian halo. A Cauchy/Exponential or Lévy

source as used in Refs.[50–53], is often adopted to account for the non-Gaussian features of the emission profile. This offers a physically intuitive interpretation of the non-Gaussian nature of the emission source. However, the results are sensitive to the choice and number of the resonances and to their momentum distributions, introducing potential model dependence. In contrast, the SF in this study is constructed using a model-independent deep neural network (DNN) approach. This approach avoids assumptions about resonance contributions and provides a more data-driven, model-independent extraction of the SF directly from experimental measurements.

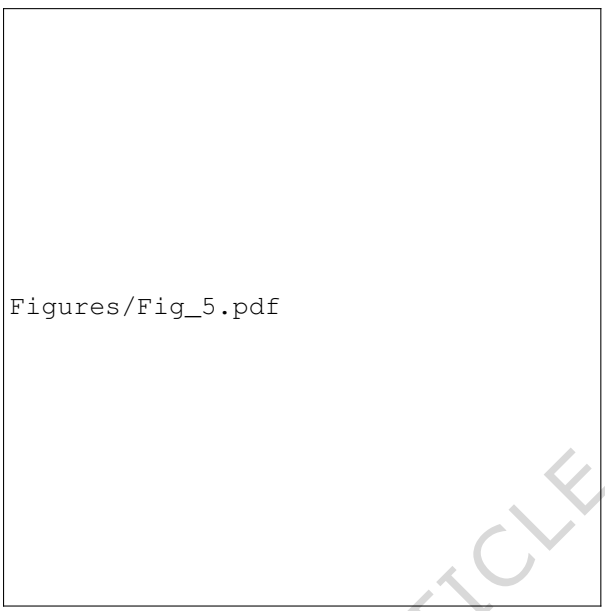

Figure 5. The correlation function of $p-\Lambda$ pairs is obtained using the Neural Network source, which was extracted based on the Av-18 potential derived from proton-proton correlations. The shaded red band corresponds to the 68% Confidence Level (CL) uncertainty. The experimental data (black dots) are from pp collisions at $\sqrt{s} = 7$ TeV, as measured by the ALICE collaboration[37].

For other hadron–hadron systems, such as $p-\Lambda$, $\Lambda-\Lambda$, and so on, the interactions are less well known. For instance, only 36 data points exist for $p-\Lambda$ scattering, measured at relatively high relative momenta and with sizable uncertainties. The interaction potential between a proton and a hyperon Λ has been described through many effective models[58–64]. The results obtained from these models are rather different, but all confirm the attractiveness of the $p-\Lambda$ interaction for low momenta. Because the mass and quark composition of a hyperon is nearly identical to those of a proton, the hadron-emitting source learned from the proton–proton correlation function can be applied to study hyperon–nucleon correlations and to investigate the $p-\Lambda$ interaction interactions. The correlation function of $p-\Lambda$ is computed assuming the interaction follows the Usmani form[58] with a parameter W_C, which determines the depth of the potential. The best agreement with experimental data is obtained for a relatively shallow potential well, $W_C = 2250$ MeV, which is consistent with preliminary lattice QCD results[64,65]. A comparison with the experimental data is presented in Fig. 5. This analysis thus provides an alternative avenue for examining and constraining the hyperon–nucleon interaction.

Conclusions

High-energy collision experiments reveal insights into the hadronic interactions, yet understanding hyperon-nucleon interactions remains limited. In this work, we employ deep neural networks within an automatic differentiation framework to reconstruct proton-emitting sources using the well-established Reid and AV18 interaction potentials. By comparison with experimental data, a non-Gaussian source function exhibiting a pronounced long-range tail is extracted. Notably, this work constitutes the first data-driven determination of a hadron-emitting source, significantly improving the extraction of hyperon–nucleon correlations, and providing a more accurate and model-independent probe of hadronic interactions via femtoscopy. We will extend this study to extract the three-dimensional hadron-emitting source in heavy-ion collisions in future.

Methods

In details, an L-layer neural network is used to represent $S_{\boldsymbol{\theta}}(r)$, with an input node r and a single output node $S_{\boldsymbol{\theta}}(r)$. The network comprises finite first-order differentiable modules, ensuring the continuity of the function $S_{\boldsymbol{\theta}}(r)$ is naturally preserved[66–68]. We adopt a default parameter setting of width $= 64$ and $L = 4$ throughout this study, with 4,224 trainable parameters in total. For optimizing the neural network representations, the Adam optimizer[69] is utilized, with a learning rate of 10^{-3} and training conducted over 10,000 epochs to approach the convergence.

Reconstruction of the source function $S(r)$ from correlation via $C(q) = \int K(q,r)S(r)\,dr$ is a first-kind *Fredholm* inversion and is routinely ill-posed in the absence of regularizations. In this work we enforce the physically mandated constraints of continuity and non-negativity by parameterizing $S(r)$ with a one-input/one-output neural network with positive activations, *Softplus*, defined as $\sigma(x) = \ln(1+e^x)$. These designs render the inverse problem well-posed; as shown in our previous analysis[56,70–72], the admissible solution space is reduced. Empirically, reconstructions from multiple random initializations converge to the same $S(r)$, corroborating uniqueness within the constrained class.

To evaluate the uncertainty of the reconstruction, a Bayesian perspective can be adopted, focusing on the posterior distribution of the SFs for the given astrophysical observations, Posterior($\boldsymbol{\theta}_{\rm SF}$|data). In this approach, an ensemble of $C(k_i)$ samples is first drawn from the normal distribution of real measurements. From this ensemble, the corresponding SFs are deterministically inferred using maximum likelihood

estimation. Given the ensemble of reconstructed SFs, importance sampling is applied to estimate the uncertainty associated with the desired posterior distribution. In this process, a proper weight is assigned to each SF to ensure accurate uncertainty quantification. Our results and uncertainty estimations in the main text adhere to this strategy. In general, a physical variable $\hat{O}$ can be estimated as:

$$\bar{O} = \langle \hat{O} \rangle = \sum_{j}^{N_{\text{samples}}} w^{(j)} O^{(j)}. \tag{9}$$

The standard deviation is given by, $(\Delta O)^2 = \langle \hat{O}^2 \rangle - \bar{O}^2$. The weights are defined as similar in Ref.[73],

$$\begin{aligned} w^{(j)} &= \frac{\text{Posterior}(\boldsymbol{\theta}_{\text{SF}}^{(j)}|\text{data})}{\text{Proposal}(\boldsymbol{\theta}_{\text{SF}}^{(j)})} \\ &\propto \frac{p(\text{data}|\boldsymbol{\theta}_{\text{SF}}^{(j)})\text{Prior}(\boldsymbol{\theta}_{\text{SF}}^{(j)})}{p(\boldsymbol{\theta}_{\text{SF}}^{(j)}|\text{samples}^{(j)})p(\text{samples}^{(j)}|\text{data})\text{Prior}(\text{data})}, \end{aligned} \tag{10}$$

where j denotes the index of a reconstructed SF (from the sampled SF ensemble), and $\boldsymbol{\theta}_{\text{SF}}$ represents the parameter set describing the SF. Here, $p(\text{samples}|\text{data}) = \mathcal{N}(C_i, \Delta C_i{}^2)$ describes the probability of samples drawn from the normal distribution of errors. Additionally, $p(\boldsymbol{\theta}_{\text{SF}}^{(j)}|\text{samples}^{(j)}) = 1$, as the reconstruction deterministically locates the corresponding SF given the sampled $C(k_i)$ points. The likelihood function, $p(\text{data}|\boldsymbol{\theta}_{\text{SF}}^{(j)}) \propto \exp(-\chi^2(C_{\boldsymbol{\theta}_{\text{SF}}^{(j)}}))$, quantifies the distances of the predicted $C(k_i)$ values from the real observations. For practical calculations, weights should be normalized as,

$$\tilde{w}^{(j)} = \frac{w^{(j)}}{\sum_j w^{(j)}}, \tag{11}$$

and a cutoff is applied to mitigate the influence of outliers in the samples. In the normalization procedure, $\text{Prior}(\boldsymbol{\theta}_{\text{SF}}^{(j)})$ and $\text{Prior}(\text{data})$ will be removed.

Data availability

The data that support the findings of this study are available from the corresponding author upon request.

Code availability

The open codes can be found in a public GitHub repository, https://github.com/Anguswlx/InferSFs.

References

1. Yukawa, H. On the Interaction of Elementary Particles I. *Proc. Phys. Math. Soc. Jap.* **17**, 48–57 (1935). DOI 10.1143/PTPS.1.1.
2. Bryan, R. A. & Scott, B. L. Nucleon-Nucleon Scattering from One-Boson-Exchange Potentials. *Phys. Rev.* **135**, B434–B450 (1964). DOI 10.1103/PhysRev.135.B434.
3. Kiang, D., Preston, M. A. & Yip, P. One-boson-exchange potential and nuclear matter. *Phys. Rev.* **170**, 907–915 (1968). URL https://link.aps.org/doi/10.1103/PhysRev.170.907. DOI 10.1103/PhysRev.170.907.
4. Lacombe, M. *et al.* Parametrization of the Paris n n Potential. *Phys. Rev. C* **21**, 861–873 (1980). DOI 10.1103/PhysRevC.21.861.
5. Wiringa, R. B., Stoks, V. G. J. & Schiavilla, R. An Accurate nucleon-nucleon potential with charge independence breaking. *Phys. Rev. C* **51**, 38–51 (1995). DOI 10.1103/PhysRevC.51.38. nucl-th/9408016.
6. Reid, R. V., Jr. Local phenomenological nucleon-nucleon potentials. *Annals Phys.* **50**, 411–448 (1968). DOI 10.1016/0003-4916(68)90126-7.
7. Stoks, V. G. J., Klomp, R. A. M., Terheggen, C. P. F. & de Swart, J. J. Construction of high quality N N potential models. *Phys. Rev. C* **49**, 2950–2962 (1994). DOI 10.1103/PhysRevC.49.2950. nucl-th/9406039.
8. Nagels, M. M., Rijken, T. A. & Yamamoto, Y. Extended-soft-core baryon-baryon model ESC16. I. Nucleon-nucleon scattering. *Phys. Rev. C* **99**, 044002 (2019). DOI 10.1103/PhysRevC.99.044002. 1408.4825.
9. Entem, D. R. & Machleidt, R. Accurate charge dependent nucleon nucleon potential at fourth order of chiral perturbation theory. *Phys. Rev. C* **68**, 041001 (2003). DOI 10.1103/PhysRevC.68.041001. nucl-th/0304018.
10. Machleidt, R. & Entem, D. R. Chiral effective field theory and nuclear forces. *Phys. Rept.* **503**, 1–75 (2011). DOI 10.1016/j.physrep.2011.02.001. 1105.2919.
11. Epelbaum, E. Few-nucleon forces and systems in chiral effective field theory. *Prog. Part. Nucl. Phys.* **57**, 654–741 (2006). DOI 10.1016/j.ppnp.2005.09.002. nucl-th/0509032.
12. Drischler, C., Hebeler, K. & Schwenk, A. Chiral interactions up to next-to-next-to-next-to-leading order and nuclear saturation. *Phys. Rev. Lett.* **122**, 042501 (2019). DOI 10.1103/PhysRevLett.122.042501. 1710.08220.
13. Hammer, H.-W., Nogga, A. & Schwenk, A. Three-body forces: From cold atoms to nuclei. *Rev. Mod. Phys.* **85**, 197 (2013). DOI 10.1103/RevModPhys.85.197. 1210.4273.
14. Gazit, D., Quaglioni, S. & Navratil, P. Three-Nucleon Low-Energy Constants from the Consistency of Interactions and Currents in Chiral Effective Field Theory. *Phys. Rev. Lett.* **103**, 102502 (2009). DOI 10.1103/PhysRevLett.103.102502. [Erratum: Phys.Rev.Lett. 122, 029901 (2019)], 0812.4444.
15. Aoki, S. Hadron interactions in lattice QCD. *Prog. Part. Nucl. Phys.* **66**, 687–726 (2011). DOI 10.1016/j.ppnp.2011.07.001. 1107.1284.

16. Iritani, T. *et al.* Systematics of the HAL QCD Potential at Low Energies in Lattice QCD. *Phys. Rev. D* **99**, 014514 (2019). DOI 10.1103/PhysRevD.99.014514. 1805.02365.

17. Yamazaki, T., Ishikawa, K.-i., Kuramashi, Y. & Ukawa, A. Study of quark mass dependence of binding energy for light nuclei in 2+1 flavor lattice QCD. *Phys. Rev. D* **92**, 014501 (2015). DOI 10.1103/PhysRevD.92.014501. 1502.04182.

18. Wagman, M. L. *et al.* Baryon-Baryon Interactions and Spin-Flavor Symmetry from Lattice Quantum Chromodynamics. *Phys. Rev. D* **96**, 114510 (2017). DOI 10.1103/PhysRevD.96.114510. 1706.06550.

19. Aoki, S. & Doi, T. *Lattice QCD and Baryon-Baryon Interactions*, 1–31 (Springer, 2023). 2402.11759.

20. Baym, G. *et al.* From hadrons to quarks in neutron stars: a review. *Rept. Prog. Phys.* **81**, 056902 (2018). DOI 10.1088/1361-6633/aaae14. 1707.04966.

21. Brown, R. H. & Twiss, R. Lxxiv. a new type of interferometer for use in radio astronomy. *The London, Edinburgh, Dublin Philos. Mag. J. Sci.* **45**, 663–682 (1954). URL https://doi.org/10.1080/14786440708520475. DOI 10.1080/14786440708520475. https://doi.org/10.1080/14786440708520475.

22. Pratt, S. Pion Interferometry for Exploding Sources. *Phys. Rev. Lett.* **53**, 1219–1221 (1984). DOI 10.1103/PhysRevLett.53.1219.

23. Lisa, M. A., Pratt, S., Soltz, R. & Wiedemann, U. Femtoscopy in relativistic heavy ion collisions. *Ann. Rev. Nucl. Part. Sci.* **55**, 357–402 (2005). DOI 10.1146/annurev.nucl.55.090704.151533. nucl-ex/0505014.

24. Alt, C. *et al.* Bose-Einstein correlations of pi-pi- pairs in central Pb+Pb collisions at A-20, A-30, A-40, A-80, and A-158 GeV. *Phys. Rev. C* **77**, 064908 (2008). DOI 10.1103/PhysRevC.77.064908. 0709.4507.

25. Li, Q.-f., Steinheimer, J., Petersen, H., Bleicher, M. & Stocker, H. Effects of a phase transition on HBT correlations in an integrated Boltzmann+Hydrodynamics approach. *Phys. Lett. B* **674**, 111–116 (2009). DOI 10.1016/j.physletb.2009.03.012. 0812.0375.

26. Wiedemann, U. A. & Heinz, U. W. Resonance contributions to HBT correlation radii. *Phys. Rev. C* **56**, 3265–3286 (1997). DOI 10.1103/PhysRevC.56.3265. nucl-th/9611031.

27. Kisiel, A., Florkowski, W. & Broniowski, W. Femtoscopy in hydro-inspired models with resonances. *Phys. Rev. C* **73**, 064902 (2006). DOI 10.1103/PhysRevC.73.064902. nucl-th/0602039.

28. Xu, J. *et al.* Imaging Freeze-Out Sources and Extracting Strong Interaction Parameters in Relativistic Heavy-Ion Collisions. *Chin. Phys. Lett.* **42**, 031401 (2025). DOI 10.1088/0256-307X/42/3/031401. 2411.08718.

29. Si, D. *et al.* Extracting Neutron-Neutron Interaction Strength and Spatiotemporal Dynamics of Neutron Emission from the Two-Particle Correlation Function. *Phys. Rev. Lett.* **134**, 222301 (2025). DOI 10.1103/PhysRevLett.134.222301. 2501.09576.

30. S.Pratt. CRAB V3.0. URL https://web.pa.msu.edu/people/pratts/freecodes/crab/home.html.

31. Mihaylov, D. L. *et al.* A femtoscopic Correlation Analysis Tool using the Schrödinger equation (CATS). *Eur. Phys. J. C* **78**, 394 (2018). DOI 10.1140/epjc/s10052-018-5859-0. 1802.08481.

32. Fabbietti, L., Mantovani Sarti, V. & Vazquez Doce, O. Study of the Strong Interaction Among Hadrons with Correlations at the LHC. *Ann. Rev. Nucl. Part. Sci.* **71**, 377–402 (2021). DOI 10.1146/annurev-nucl-102419-034438. 2012.09806.

33. Adams, J. *et al.* Proton - lambda correlations in central Au+Au collisions at S(NN)**(1/2) = 200-GeV. *Phys. Rev. C* **74**, 064906 (2006). DOI 10.1103/PhysRevC.74.064906. nucl-ex/0511003.

34. Adam, J. *et al.* The Proton-Ω correlation function in Au+Au collisions at $\sqrt{s_{NN}}$=200 GeV. *Phys. Lett. B* **790**, 490–497 (2019). DOI 10.1016/j.physletb.2019.01.055. 1808.02511.

35. Adamczyk, L. *et al.* ΛΛ Correlation Function in Au+Au collisions at $\sqrt{s_{NN}} = 200$ GeV. *Phys. Rev. Lett.* **114**, 022301 (2015). DOI 10.1103/PhysRevLett.114.022301. 1408.4360.

36. Adamczyk, L. *et al.* Measurement of Interaction between Antiprotons. *Nat.* **527**, 345–348 (2015). DOI 10.1038/nature15724. 1507.07158.

37. Acharya, S. *et al.* p-p, p-Λ and Λ-Λ correlations studied via femtoscopy in pp reactions at $\sqrt{s} = 7$ TeV. *Phys. Rev. C* **99**, 024001 (2019). DOI 10.1103/PhysRevC.99.024001. 1805.12455.

38. Acharya, S. *et al.* Experimental Evidence for an Attractive p-ϕ Interaction. *Phys. Rev. Lett.* **127**, 172301 (2021). DOI 10.1103/PhysRevLett.127.172301. 2105.05578.

39. Acharya, S. *et al.* Investigation of the p–Σ0 interaction via femtoscopy in pp collisions. *Phys. Lett. B* **805**, 135419 (2020). DOI 10.1016/j.physletb.2020.135419. 1910.14407.

40. Acharya, S. *et al.* First Observation of an Attractive Interaction between a Proton and a Cascade Baryon. *Phys. Rev. Lett.* **123**, 112002 (2019). DOI 10.1103/PhysRevLett.123.112002. 1904.12198.

41. Acharya, S. *et al.* First measurement of the Λ–Ξ interaction in proton–proton collisions at the

LHC. *Phys. Lett. B* **844**, 137223 (2023). DOI 10.1016/j.physletb.2022.137223. 2204.10258.

42. Lednicky, R. & Lyuboshits, V. L. Final State Interaction Effect on Pairing Correlations Between Particles with Small Relative Momenta. *Yad. Fiz.* **35**, 1316–1330 (1981).

43. Ohnishi, A., Morita, K., Miyahara, K. & Hyodo, T. Hadron–hadron correlation and interaction from heavy–ion collisions. *Nucl. Phys. A* **954**, 294–307 (2016). DOI 10.1016/j.nuclphysa.2016.05.010. 1603.05761.

44. Kisiel, A. Non-identical particle femtoscopy at s(NN)**(1/2) = 200-AGeV in hydrodynamics with statistical hadronization. *Phys. Rev. C* **81**, 064906 (2010). DOI 10.1103/PhysRevC.81.064906. 0909.5349.

45. Sinyukov, Y. M., Shapoval, V. M. & Naboka, V. Y. On m_T dependence of femtoscopy scales for meson and baryon pairs. *Nucl. Phys. A* **946**, 227–239 (2016). DOI 10.1016/j.nuclphysa.2015.11.014. 1508.01812.

46. Csorgo, T., Hegyi, S. & Zajc, W. A. Bose-Einstein correlations for Levy stable source distributions. *Eur. Phys. J. C* **36**, 67–78 (2004). DOI 10.1140/epjc/s2004-01870-9. nucl-th/0310042.

47. Aamodt, K. *et al.* Femtoscopy of pp collisions at $\sqrt{s} =$ 0.9 and 7 TeV at the LHC with two-pion Bose-Einstein correlations. *Phys. Rev. D* **84**, 112004 (2011). DOI 10.1103/PhysRevD.84.112004. 1101.3665.

48. Adam, J. *et al.* Two-pion femtoscopy in p-Pb collisions at $\sqrt{s_{\rm NN}} = 5.02$ TeV. *Phys. Rev. C* **91**, 034906 (2015). DOI 10.1103/PhysRevC.91.034906. 1502.00559.

49. Acharya, S. *et al.* Search for a common baryon source in high-multiplicity pp collisions at the LHC. *Phys. Lett. B* **811**, 135849 (2020). DOI 10.1016/j.physletb.2020.135849. 2004.08018.

50. Acharya, S. *et al.* Common femtoscopic hadron-emission source in pp collisions at the LHC (2023). 2311.14527.

51. Sirunyan, A. M. *et al.* Bose-Einstein correlations in pp, pPb, and PbPb collisions at $\sqrt{s_{NN}} = 0.9 - 7$ TeV. *Phys. Rev. C* **97**, 064912 (2018). DOI 10.1103/PhysRevC.97.064912. 1712.07198.

52. Sirunyan, A. M. *et al.* Bose-Einstein correlations of charged hadrons in proton-proton collisions at $\sqrt{s} = 13$ TeV. *JHEP* **03**, 014 (2020). DOI 10.1007/JHEP03(2020)014. 1910.08815.

53. Aad, G. *et al.* Two-particle Bose–Einstein correlations in pp collisions at $\sqrt{\mathbf{s}} = 0.9$ and 7 TeV measured with the ATLAS detector. *Eur. Phys. J. C* **75**, 466 (2015). DOI 10.1140/epjc/s10052-015-3644-x. 1502.07947.

54. Day, B. D. Three-body correlations in nuclear matter. *Phys. Rev. C* **24**, 1203–1271 (1981). DOI 10.1103/PhysRevC.24.1203.

55. Ohnishi, A. *Hadrons, Quark-Gluon Plasma, and Neutron Stars*, 1–58 (Springer, 2023).

56. Aarts, G. *et al.* Physics-driven learning for inverse problems in quantum chromodynamics. *Nat. Rev. Phys.* (2025). DOI 10.1038/s42254-024-00798-x.

57. Bishop, C. M. & Bishop, H. *Deep learning: Foundations and concepts* (Springer Nature, 2023).

58. Bodmer, A. R., Usmani, Q. N. & Carlson, J. BINDING ENERGIES OF HYPERNUCLEI AND THREE-BODY LAMBDA N N FORCES. *Phys. Rev. C* **29**, 684–687 (1984). DOI 10.1103/PhysRevC.29.684.

59. Rijken, T. A. & Yamamoto, Y. Extended-soft-core baryon-baryon model. II. Hyperon-nucleon interaction. *Phys. Rev. C* **73**, 044008 (2006). DOI 10.1103/PhysRevC.73.044008. nucl-th/0603042.

60. Sasaki, K., Oset, E. & Vicente Vacas, M. J. Scalar Lambda N and Lambda Lambda interaction in a chiral unitary approach. *Phys. Rev. C* **74**, 064002 (2006). DOI 10.1103/PhysRevC.74.064002. nucl-th/0607068.

61. Polinder, H., Haidenbauer, J. & Meissner, U.-G. Hyperon-nucleon interactions: A Chiral effective field theory approach. *Nucl. Phys. A* **779**, 244–266 (2006). DOI 10.1016/j.nuclphysa.2006.09.006. nucl-th/0605050.

62. Nagels, M. M., Rijken, T. A. & Yamamoto, Y. Extended-soft-core baryon-baryon model ESC16. II. Hyperon-nucleon interactions. *Phys. Rev. C* **99**, 044003 (2019). DOI 10.1103/PhysRevC.99.044003. 1501.06636.

63. Haidenbauer, J. *et al.* Hyperon-nucleon interaction at next-to-leading order in chiral effective field theory. *Nucl. Phys. A* **915**, 24–58 (2013). DOI 10.1016/j.nuclphysa.2013.06.008. 1304.5339.

64. Nemura, H. Lambda-Nucleon and Sigma-Nucleon potentials from space-time correlation function on the lattice. *PoS* **LATTICE2021**, 272 (2022). DOI 10.22323/1.396.0272. 2203.07661.

65. Wang, F.-q. & Pratt, S. Lambda proton correlations in relativistic heavy ion collisions. *Phys. Rev. Lett.* **83**, 3138–3141 (1999). DOI 10.1103/PhysRevLett.83.3138. nucl-th/9907019.

66. Wu, L., Zhu, Z. & E, W. Towards Understanding Generalization of Deep Learning: Perspective of Loss Landscapes. *arXiv e-prints* arXiv:1706.10239 (2017). 1706.10239.

67. Rosca, M., Weber, T., Gretton, A. & Mohamed, S. A case for new neural network smoothness constraints. In Zosa Forde, J., Ruiz, F., Pradier, M. F. & Schein, A. (eds.) *Proceedings on "I Can't Believe It's Not Better!" At NeurIPS Workshops*, vol. 137 of *Proceedings of Machine Learning Research*, 21–32 (PMLR, 2020). URL https://proceedings.mlr.press/v137/rosca20a.html.

68. Shi, S., Wang, L. & Zhou, K. Rethinking the ill-posedness of the spectral function reconstruction — Why is it fundamentally hard and how Artificial Neural Networks can help. *Comput. Phys. Commun.* **282**, 108547 (2023). DOI 10.1016/j.cpc.2022.108547. 2201.02564.

69. Kingma, D. P. & Ba, J. Adam: A method for stochastic optimization. *arXiv preprint arXiv:1412.6980* (2014).

70. Wang, L., Shi, S. & Zhou, K. Automatic differentiation approach for reconstructing spectral functions with neural networks. In *35th Conference on Neural Information Processing Systems* (2021). 2112.06206.

71. Shi, S., Zhou, K., Zhao, J., Mukherjee, S. & Zhuang, P. Heavy quark potential in the quark-gluon plasma: Deep neural network meets lattice quantum chromodynamics. *Phys. Rev. D* **105**, 014017 (2022). DOI 10.1103/PhysRevD.105.014017. 2105.07862.

72. Wang, L., Shi, S. & Zhou, K. Reconstructing spectral functions via automatic differentiation. *Phys. Rev. D* **106**, L051502 (2022). DOI 10.1103/PhysRevD.106.L051502. 2111.14760.

73. Soma, S., Wang, L., Shi, S., Stöcker, H. & Zhou, K. Reconstructing the neutron star equation of state from observational data via automatic differentiation. *Phys. Rev. D* **107**, 083028 (2023). DOI 10.1103/PhysRevD.107.083028. 2209.08883.

Acknowledgements

We thank Drs. Takumi Doi, Tetsuo Hatsuda, and Zhigang Xiao for helpful discussions. We thank the DEEP-IN working group at RIKEN-iTHEMS for support in the preparation of this paper. LW is supported by the RIKEN TRIP initiative (RIKEN Quantum), JSPS KAKENHI Grant No. 25H01560, and JST-BOOST Grant No. JPMJBY24H9. JX is support by the Deutsche Forschungsgemeinschaft (DFG, German Research Foundation) through the grant CRC-TR 211 'Strong-interaction matter under extreme conditions' - Project number 315477589 - TRR 211.

Author contributions

Both Dr. Jiaxing Zhao and Dr. Lingxiao Wang contributed equally to all aspects of the article.

Competing interests

The authors declare no competing interests.

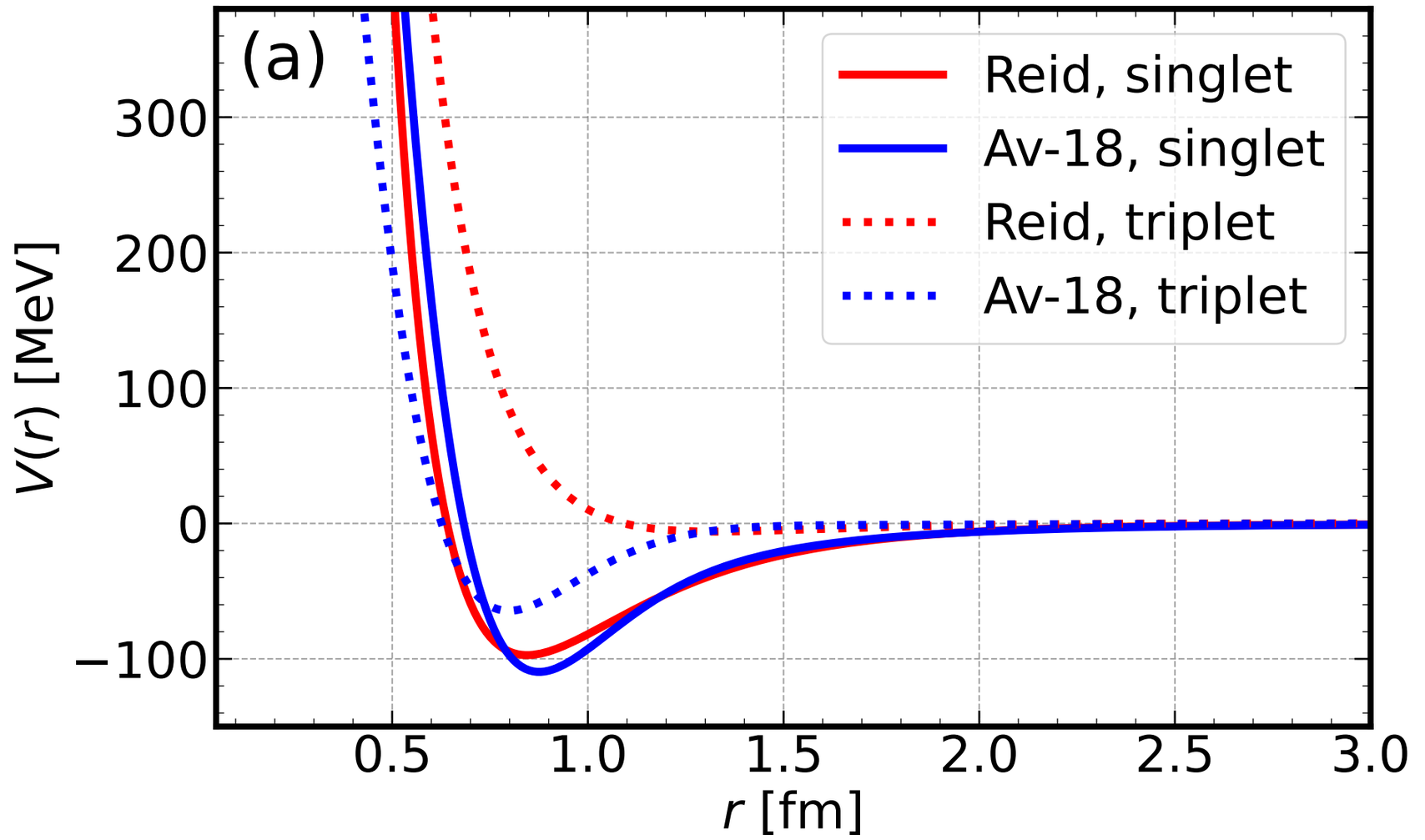
(a)
Reid, singlet
Av-18, singlet
Reid, triplet
Av-18, triplet
V(r) [MeV]
300
200
100
0
−100
0.5
1.0
1.5
2.0
2.5
3.0
r [fm]

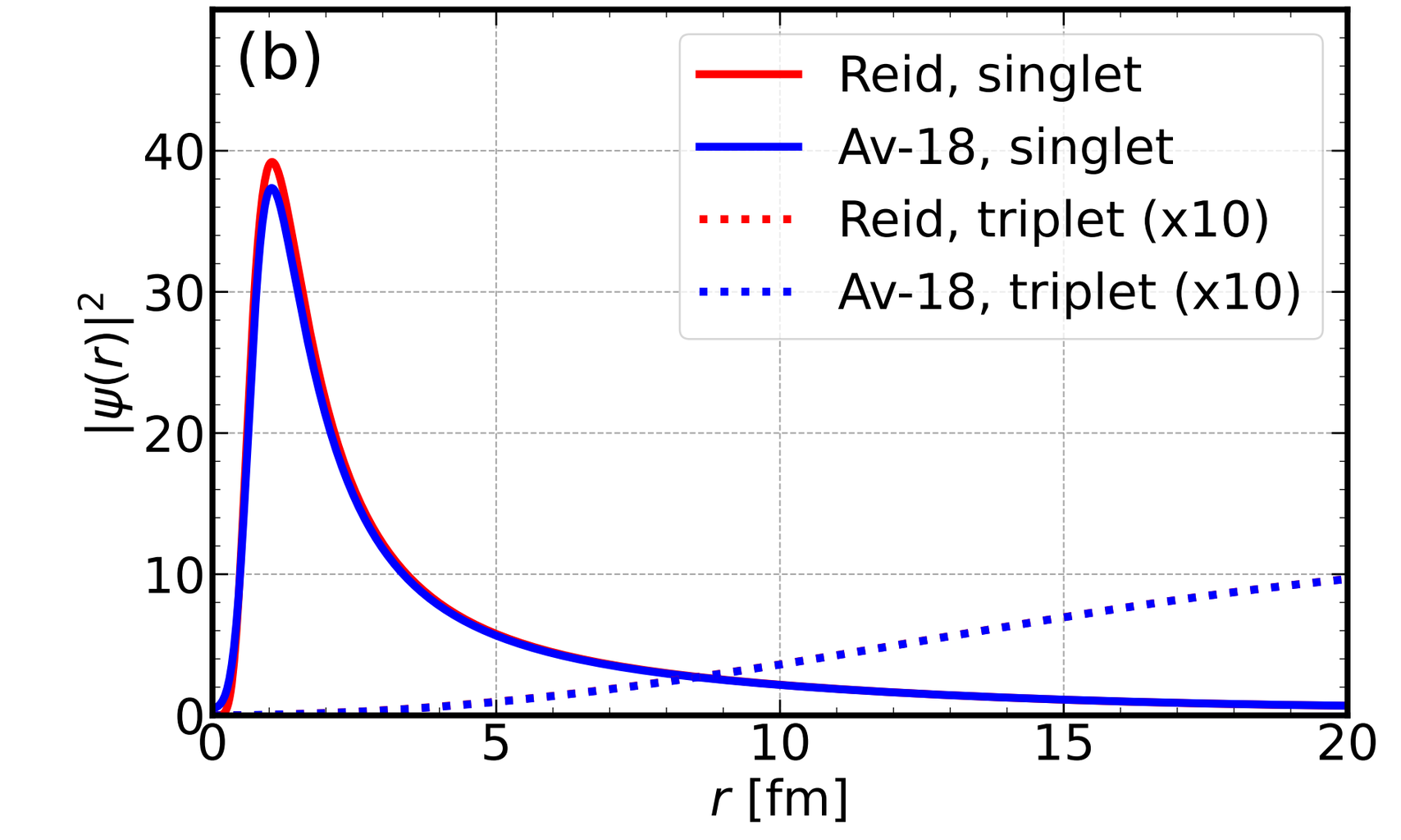
(b)
Reid, singlet
Av-18, singlet
Reid, triplet (x10)
Av-18, triplet (x10)
|ψ(r)|²
40
30
20
10
0
0
5
10
15
20
r [fm]

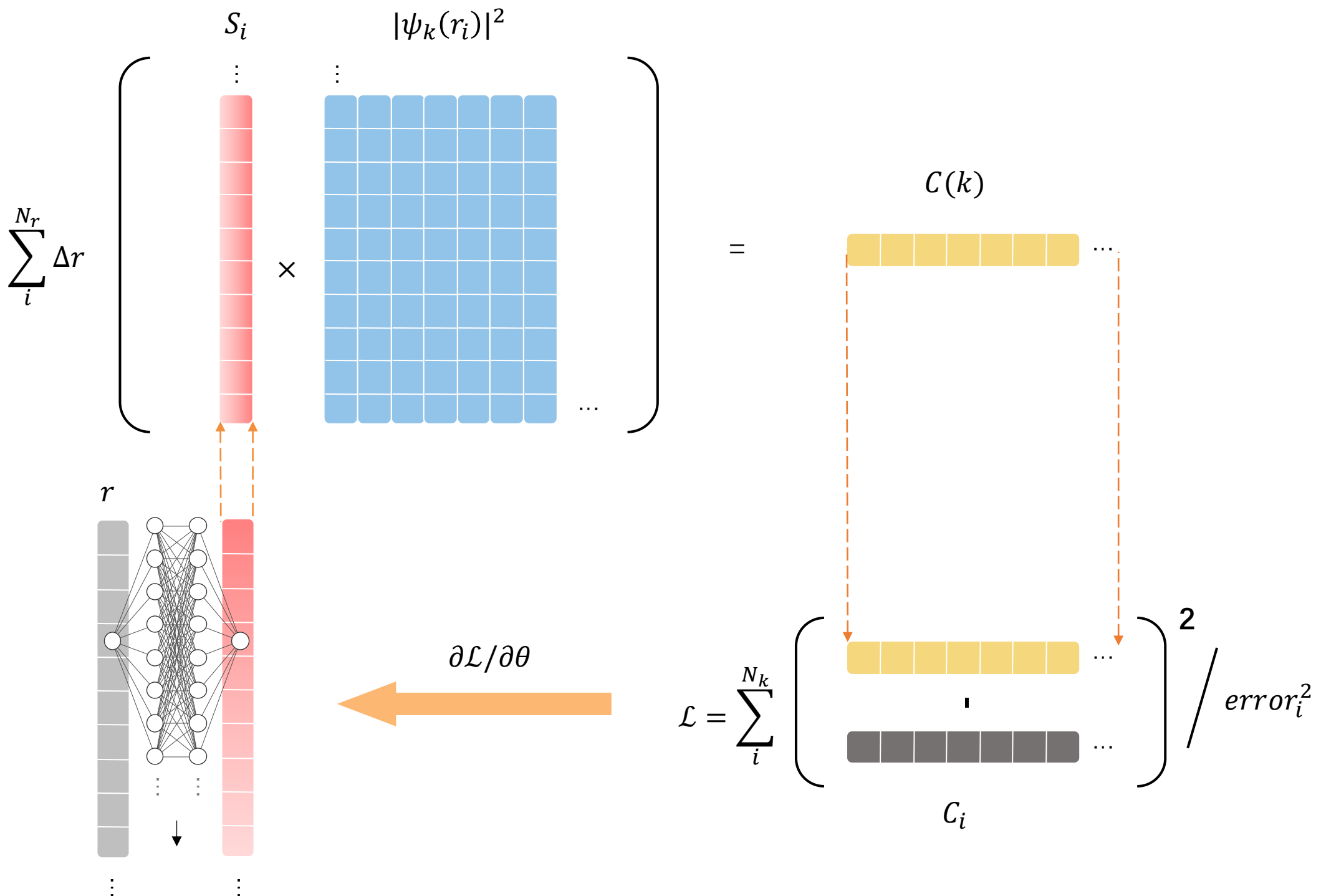
S_i
$|\psi_k(r_i)|^2$
$\sum_i^{N_r} \Delta r$
×
=
$C(k)$
r
$\partial\mathcal{L}/\partial\theta$
$\mathcal{L} = \sum_i^{N_k}$
$error_i^2$
C_i

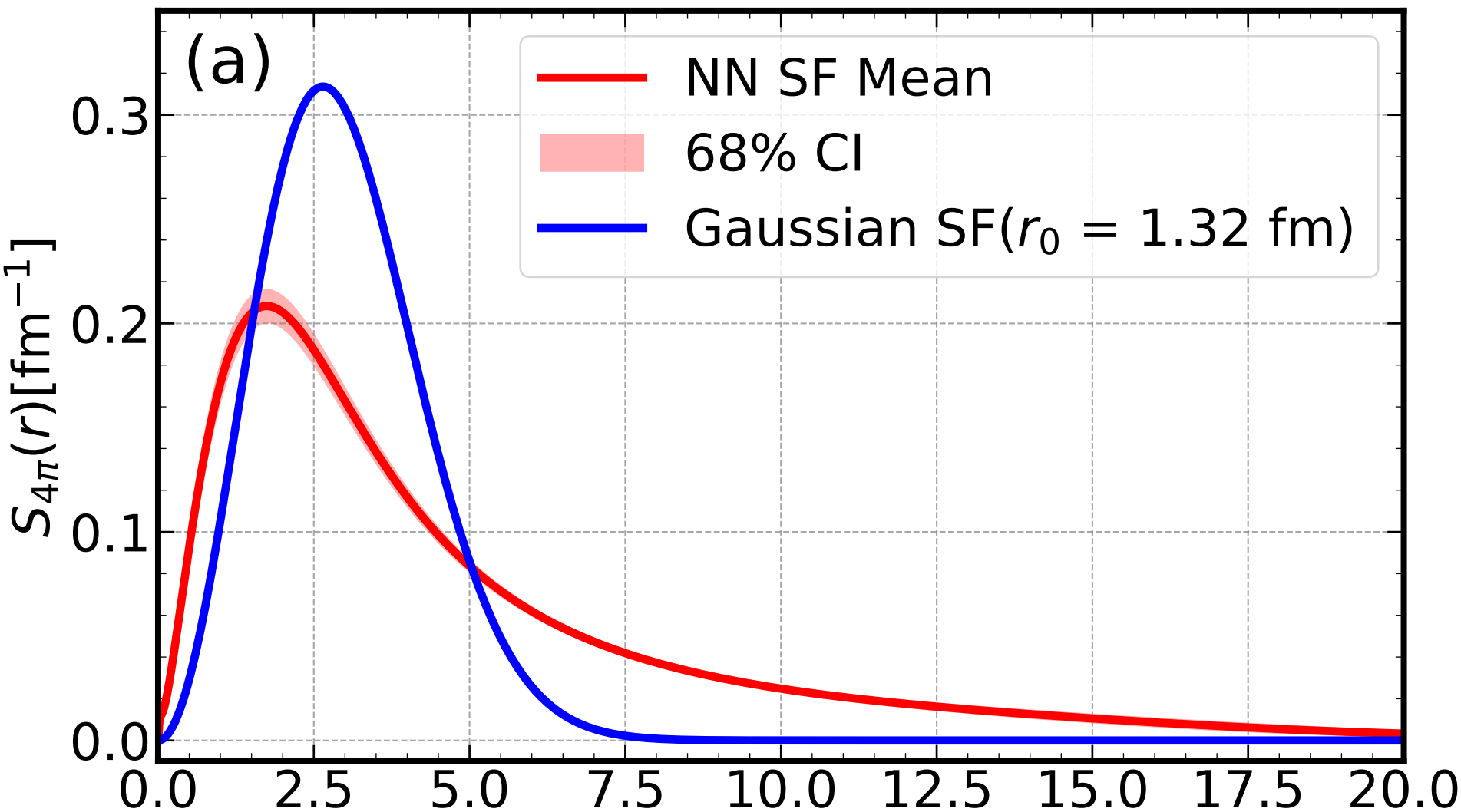
(a)
NN SF Mean
68% CI
Gaussian SF(r_0 = 1.32 fm)
$S_{4\pi}(r)$[fm^{-1}]
0.0
0.1
0.2
0.3
0.0
2.5
5.0
7.5
10.0
12.5
15.0
17.5
20.0
r [fm]

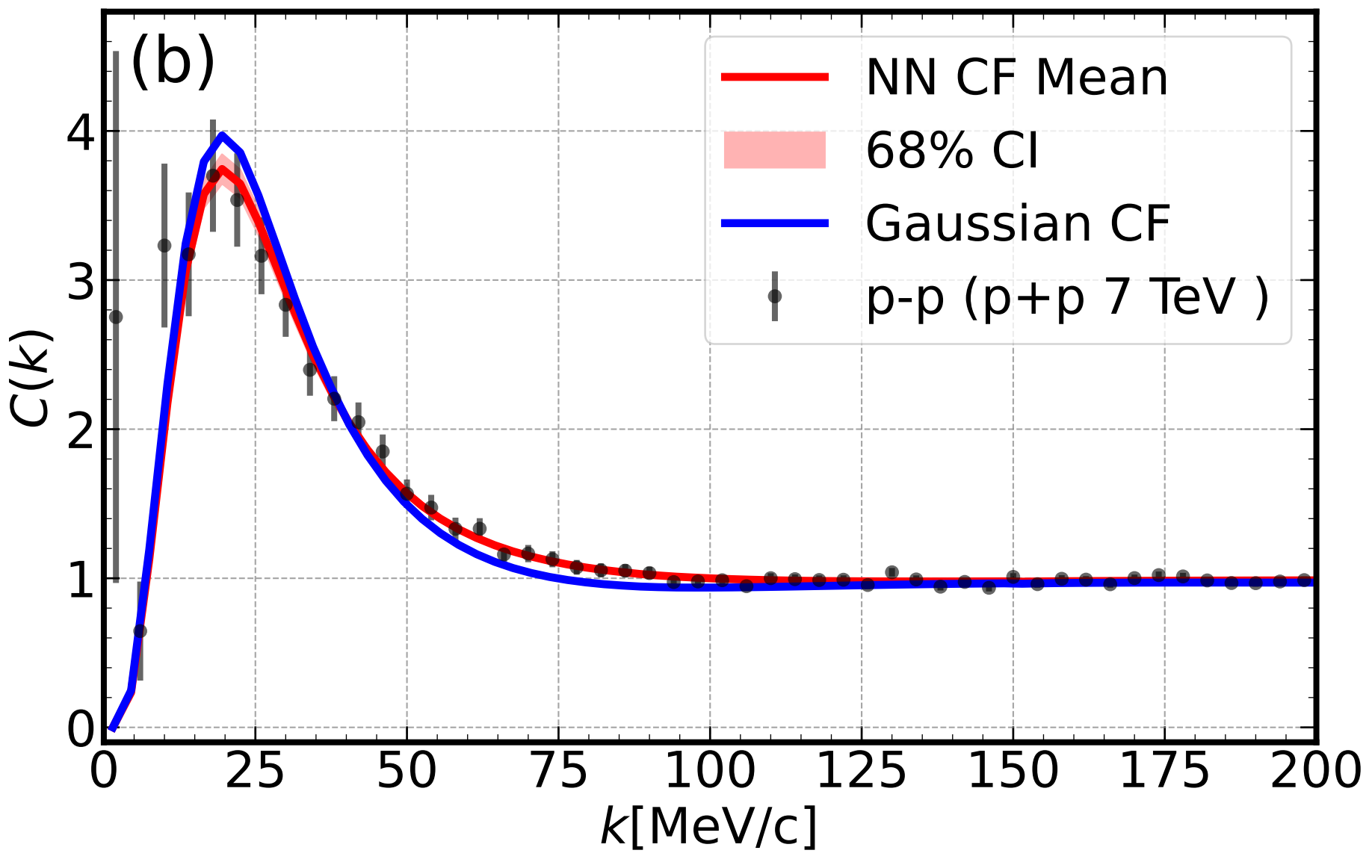
(b)
NN CF Mean
68% CI
Gaussian CF
p-p (p+p 7 TeV)
$C(k)$
0
1
2
3
4
0
25
50
75
100
125
150
175
200
k[MeV/c]

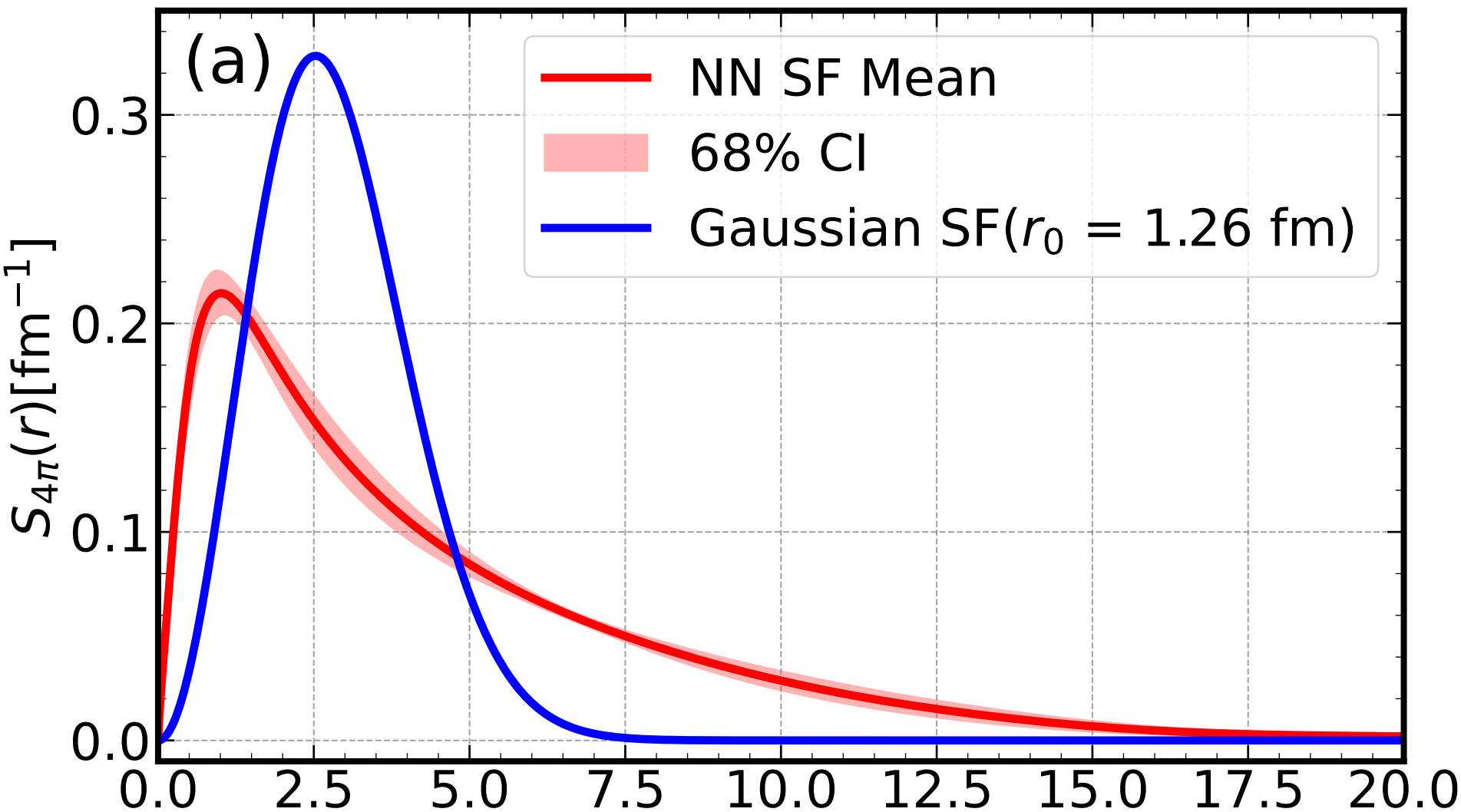
(a)
NN SF Mean
68% CI
Gaussian SF(r_0 = 1.26 fm)
$S_{4\pi}(r)$[fm^{-1}]
0.0
0.1
0.2
0.3
0.0
2.5
5.0
7.5
10.0
12.5
15.0
17.5
20.0
r [fm]
(b)
NN CF Mean
68% CI
Gaussian CF
p-p (p+p 7 TeV)
$C(k)$
0
1
2
3
4
0
25
50
75
100
125
150
175
200
k[MeV/c]

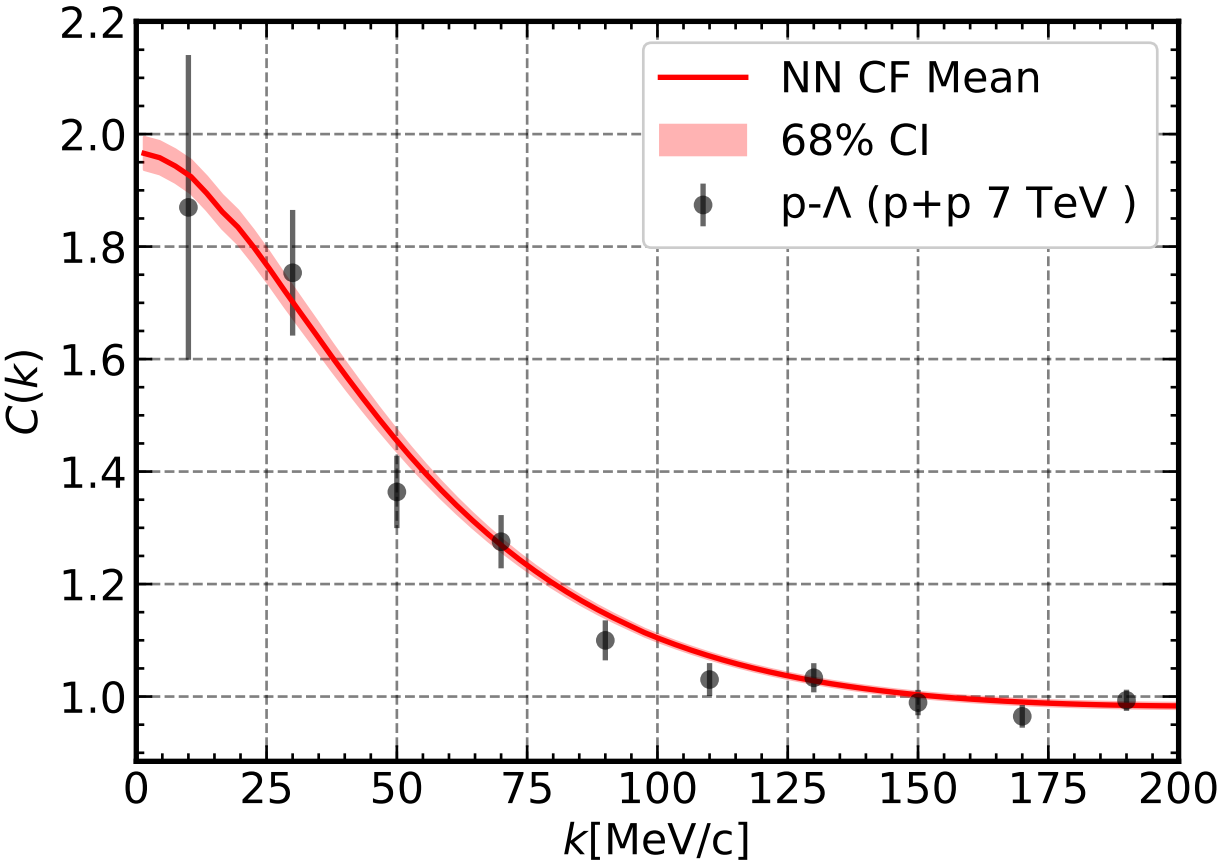
NN CF Mean
68% CI
p-Λ (p+p 7 TeV)
C(k)
k[MeV/c]
2.2
2.0
1.8
1.6
1.4
1.2
1.0
0
25
50
75
100
125
150
175
200